City Research Online

Citation: Ostmann, S., Chaves, H. & Bruecker, C. (2017). Path instabilities of light particles rising in a liquid with background rotation. Journal of Fluids and Structures, 70, pp. 403-416. doi: 10.1016/j.jfluidstructs.2017.02.007

Path instabilities of light particles rising in a liquid with background rotation

S. Ostmann,*[1)] H. Chaves[1)] and C. Brücker[2)]

[1)] *Institute for Mechanics and Fluid Dynamics, TU Bergakademie Freiberg, Lampadiusstraße 4, 09596, Freiberg, Germany*
[2)] *School of Mathematics, Computer Science and Engineering, City University London*
**stefan.ostmann@imfd.tu-freiberg.de*

Abstract

The present paper reports on experimental observations performed on 2-6 millimeter low-density polystyrene particles rising freely in a water-glycerol mixture for the liquid at rest as well as with slow background rotation (axisymmetric solid body rotation around the vertical axis). Particle trajectories were studied in the Reynolds-numbers range of 200 < Re < 800 at a fixed rotation rate of Ω=0.8 1/s. Both the trajectory measurements and the wake visualization indicate that there are differences in the wake structure of the particles as well as in the path instabilities compared to those in quiescent fluid. In the swirling flow, the two-threaded wake mode is dominant up to Reynolds numbers of about 500 with typical spiral-type trajectories until vortex shedding commences. In contrast, under quiescent flow conditions vortex shedding already occurs above Re=230, and the particles predominantly move in zig-zagging paths. Thus, the presence of background rotation is able to suppress vortex shedding and to delay the transition. For the co-rotating observer, the radius of the spiral-type path is comparable to that of the transversal motion under quiescent flow conditions. Therefore, the magnitude of lateral lift-forces is not greatly affected by the presence of the swirl.

I.Introduction

The occurrence of path instabilities in free rising or falling particles was a widely investigated field over the last few decades, a recent review is given in *Ern et. al.*[1]. The origin of these path instabilities are forces acting perpendicularly to the main direction of motion. These forces are generally referred to as “lift forces”. Important effects contributing to these lateral lift forces have been investigated by *Auton et. al.*[2] under inviscid conditions assuming the motion of bluff bodies or cylinders in a large scale, non-uniform, rotational flow using an analytical approach. These investigations pointed out the importance of the contributions made by the bodies added mass. *Auton et. al.* [2] additionally stated that there is an additional force induced by the ambient background rotation that could be added to the previously mentioned forces under the conditions of inviscid flow, whereupon its contribution to the lift-force is relatively low, compared to the inertia- and bound-vorticity-caused lift forces. The contribution of the bound vorticity, produced by the body, is extensively discussed in *Horrowitz et. al.*[3] and *Magnaudet et. al.*[4]. The latter stated that these are the "root of the (path) instabilities". The experimental wake visualizations by, e.g., *DeVries et. al.*[5] and *Veldhuis et. al.*[6,7], indicated that path instabilities are linked to the transport of bound-vorticity into the wake; this demonstrates the influence of viscous effects on the lateral motion.

According to the above mentioned authors, the acting lateral forces are caused by a number of sources including viscous, added mass, bound-vorticity and background vorticity associated effects, which affect each other and could therefore not be broken down or described separately from each other (e.g. see *Sarpkaya et. al.*[8]). Subject to this dilemma is also that numerical simulations following different models for the lift forces sometimes lead to diametrical results. This is particularly evident in the surprising results of *Sridhar & Katz et. al.*[9], who examined the lift forces of small bubbles in experimental trials in flow fields with different types of shear fields (plane shear flow, vortex flow). They found that the flow-induced lift forces on the bubbles in the case of the vortex field are larger than those in a planar shear field at the same dimensionless velocity gradient by an order of magnitude in both velocity fields. Recent direct numerical simulations of the flow around a stationary sphere in simple base-flow by *Bagchi & Balachandar*[10] for Reynolds numbers of the particle flow around $100 < Re < 1000$ found that the shear-induced and the vorticity-induced component of the lift force exhibit varying influences. The latter is a friction-related contribution, which increases in proportion to the slip-velocity in the circumferential direction and is controlled by the wall-shear stress distribution around the body. By allowing a self-rotation of the sphere in accordance with the ambient vorticity, the numerical result does not change significantly; thus, the rotation-related Magnus effect appears to be of minor importance. The direction of this viscous lift-force component is pointing away from the vortex center; this resulted in the statement of *Bagchi & Balachandar*[10] that theoretically smaller bubbles in bubbly flows do not necessarily move toward the axis of a vortex. Recent experimental studies for the bubble behavior under influence of ambient vorticity were conducted by *Bluemink et. al.*[11]. They used a spinning vessel with horizontal rotation axis to keep different spheres levitated in the observer field. This allowed investigation of the occurring forces under approximately steady state conditions, where only the occurring fluctuation of the vortex induced lift-forces lead a path instability observed as orbits of differing diameters around the rotation axis.

This situation is completely different than a setup in which the gravitational force is perpendicular to the rotation axis, is totally different. Consequently, the studies of the particle wake structure did not exhibit striking similarities to the available literature. Generally speaking, the occurring wake instabilities are very probably the basic cause of the path instabilities that have been frequently observed (see *Ern et. al*[1]). *Horowitz et. al.*[3] also noticed that the bodies paths are also dramatically changing with respect to the background noise: a constantly rotating background, for example, could be considered a special case of this. To date there is no information on the influence of such low background rotation on the bodies paths and the corresponding path instabilities. The present study aims to contribute to the clarification of this.

Several studies on bubble path instabilities have already investigated this for quiescent conditions, see e.g. *Magnaudet et. al.*[4], *Ellingsen et. al.*[12] and *Shew et. al.*[13]. These studies revealed that there is a transition in the bubble rise with increasing bubble diameter from a rectilinear path to an oscillation in a transversal plane (zig-zagging) to evolve into a helical path. Detailed PIV measurements by *Brücker et. al.*[14] documented the regular shedding of hairpin-like vortices that corresponds to the zig-zagging behavior; this pointed to the strong relation between wake instabilities and the induced lateral motion. In addition, a study of the wake of a solid sphere showed the exact balancing of two counter-rotating helical vortices responsible for these planar wake oscillations (*Brücker et. al.*[15]). If one of these waves is growing against the other, the wake starts to twist; this was interpreted as one explanation of the transition from zig-zagging to spiral-type trajectories (*Brücker et. al.*[14]). Wake visualization studies by *DeVries*[5] showed these transitions in the Reynolds range from 200 to 800, where the first vorticity is convecting continuously into the wake, thus forming a two threaded wake consisting of two counter rotating vortices (Re < 250). the periodical shedding of hairpin vortices and zig-zagging evolves from this state. Finally, the bubble exhibits a rocking behavior with irregular shedding (Re > 800). The present study's aim is to investigate the influence of an ambient vorticity field on that transition. For that reason, a number of light particles were analyzed with respect to their resulting particle trajectory in a water-glycerol mixture with solid body rotation. Light particles in dense fluids are well posed for such experiments as they allow observation of the path instabilities under well controlled conditions and thus allow conclusions to be drawn about the involved lift-forces. This requires a sufficiently low density ratio between the particle and the surrounding fluid of less than 0.2; otherwise amplitudes of the flow-induced particle path instabilities will greatly reduced (*DeVries et. al.*[5]). The general aim of the present study is an empirical investigation of possible influences of ambient vorticity to path instabilities during the buoyancy driven particle ascent.

II.Experimental Setup and conditions

The experimental setup consists of a transparent polyacrylic vessel (inner diameter of D_{Vessel} = 0.48 m, height of 0.8 m) filled with liquid (water-glycerol mixture, mixing ratio 40 vol-%, density ρ = 1.103 g/cm³, kinematic viscosity ν= 2.8e-6 m²/s) and mounted on an axial bearing. The vessel is spun around the vertical axis by a belt drive on the upper shell. In the present study, the rotational frequency was fixed to Ω=0.8 1/s. For these experiments, approximately spherical polystyrene particles with equivalent diameter *D* in the range 2-6 mm were used. The sphericity of the particles was measured prior to the experiments using a transmitted light setup and considering multiple perspectives. Figure 1 shows a set of sample images of one of the particles used. The sphericity parameter *s* was computed as the standard deviation of the particles diameter.

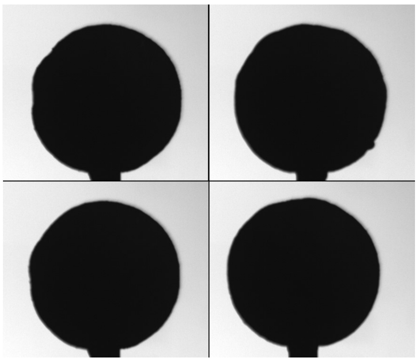

Figure 1. Sample Images of particle G (D=5.23 mm, S=1.4%).

The particle mass was measured using microgram scale (accuracy 10 µg), and the single particle volume was verified with a pygnometer. From both the density of the solid particle ρ_S is determined. The non-dimensional parameters of the problem are the Galilei-, the Reynolds- and the Rossby number, given in eq. (1), defined with the terminal rise velocity U and the rotation rate Ω.

$$\mathrm{Re} = \frac{\mathrm{D}\cdot \mathrm{u}_T}{\nu}, \qquad \mathrm{Ro} = \frac{\mathrm{u}_T}{\Omega\cdot \mathrm{D}}, \qquad \mathrm{Ga} = \frac{\mathrm{D}\cdot\sqrt{D\left(1-\frac{\rho_P}{\rho}\right)\mathrm{g}}}{\nu} \tag{1}$$

Table 1 shows the resulting values for the non-dimensional parameters Re (without background rotation), Re* (with background rotation), Ga, Ro along with the density ratio σ_s/σ, and the mean vertical velocities with (U_t*) and without background rotation (u_t).

For wake visualization, the particles were coated with a thin water-soluble layer of a sugar-dye mixture (Allura Red, AC, absorption peak wavelength at 520 nm). Prior to the experiment, the particles are filled into a revolving magazine at the bottom of the vessel, which is operated by a servo motor. The drum magazine is covered by a stationary cap with a circular opening, which is centered with the vessel rotation axis. When a magazine chamber with a particle inside reaches the circular hole, the particle is released. A step-wise revolution is controlled from the outside by infrared pulses; thus, a single particle can be released with each pulse.

Due to varying diameters of the particles in the magazine chamber, there is an uncertainty of the ejection position relative to the vessel rotation center. This resulting uncertainty could be expressed relatively to the diameter of the rotating vessel D_{Vessel} and the diameter of the particle outlet a by:

$$e_r = \frac{a - \frac{D}{2}}{D_{Vessel}} \cdot 100\% \tag{2}$$

Which yields an error of the ejection position in relation to the vessels diameter lower than 2%.

Table 1. Parameter values of investigated Particle set, sorted with increasing Re-number.

Particle	D *mm*	s *%*	U_t *m/s*	U_t^* *m/s*	ρ_s/ρ -	Ga -	Re -	Re^* -	Ro -
A	2.49	2.9	0.1978	0.1911	0.068	130	182	184	94.3
B	3.43	3.8	0.2128	0.1981	0.041	223	291	278	70.9
C	3.54	2.3	0.2194	0.2088	0.024	210	273	257	72.5
D	3.95	2.0	0.2335	0.2189	0.034	250	356	328	68.0
E	3.82	1.9	0.2441	0.2261	0.029	262	347	316	72.5
F	4.27	2.3	0.2718	0.2444	0.023	295	436	398	70.4
G	5.23	1.4	0.2813	0.2761	0.029	402	556	535	64.9
H	6.4	1.6	0.3244	0.2994	0.032	545	809	733	57.5

Additionally fluctuations of the parabolic surface during rotation were detected, which are possibly caused by slight precessions of the rotation axis within the order 1-2°. Assuming a nearly vertical rotation axis this yields a periodic shift of the rotation axis relatively to the particle outlet, and therefore the ejected particles experience slightly differing horizontal slip velocities.

The 3D trajectory measurements were performed with a stereo-shadowgraphy imaging-system. The principle setup is illustrated within Figure 2. The measurement setup consists of two CMOS Cameras (mv BlueCougar, 1000x1600 Pixel resolution, 180 fps) equipped with f=15mm lenses and arranged in perpendicular viewing directions. Illumination was achieved by two pulsed green high power LED light sources (emission peak wavelength 530 nm) mounted at a 90 degree angle close to the cameras, emitting light through a tilted beam splitter plate into the optical path of the system. The light is reflected 90 degrees into the measurement system, passes through the measurement volume and is reflected by a retroreflective layer back into the camera lens (*Settles*[16]). The field of view in the region of interest was B×H = 14×30 cm^2 (B = width, H = height), at which the larger dimension was oriented in the direction of the buoyancy-driven particle rise. The field of view is located between 80 and 380 mm above the particle outlet.

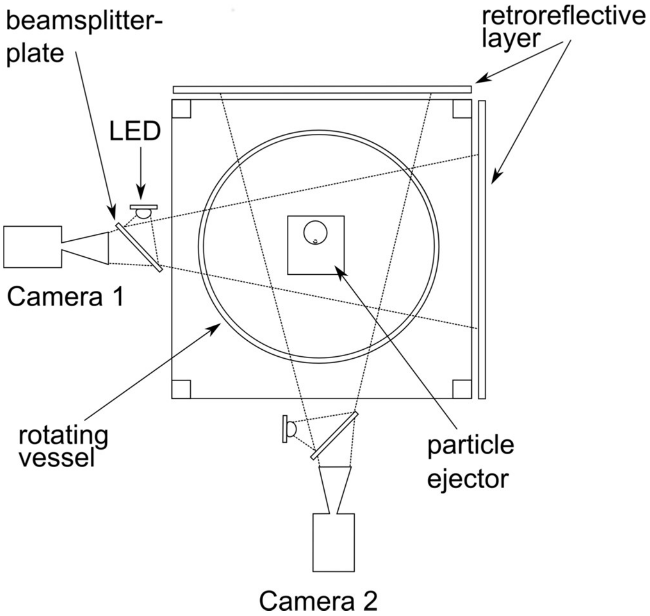

Figure 2. Experimental setup using stereo shadowgraphy.

Image acquisition starts slightly before and ends shortly after the particle enters and leaves the field of view. The particle images were refined using background division and histogram adjustment to obtain maximum contrast. The camera system was calibrated using a checkerboard target moved with a stepper motor in 2.5 mm steps in the direction of depth. The utilized calibration algorithm follows the procedure of *Soloff et. al.*[17] using two polynomials with 3rd order dependence in physical x, z dimension (co parallel to X-Z-camera plane of one camera) and 2nd order dependence in direction of depth (physical y-direction). This allows determination of the line of sight for every pixel in both camera planes, see *Kühn*[18]. Triangulation of the particle image centroids in both views then leads to the 3D position of the particle in the vessel. The optical resolution of this setup is 90 µm/pixel in the center plane, while the disparity error was found to be less than 0.5 Pixel; this yields a triangulation error originating from the triangulation process of less than 100 µm. Due to slight imperfections in particle shape and illumination, an additional uncertainty in the particle center position arises. This error is directly proportional to the particles shape deviations measured prior to the experiments; thus, the final triangulation uncertainty is within the range of less than 10% of the particle diameter. Defects in the vessel walls sometimes lead to detection of ghost particles, which are identified by comparing the physical distance to the rest of the trajectory. The results of the image processing and triangulation routines are sets of 3D point data along the trajectory of the particle.

III.Data Post Processing

Trajectory evaluation for an observation in the co-rotating reference frame

The trajectories obtained in the presence of background rotation not only exhibit particle path instabilities, but the motion is also superposed with a helical path originating from any eccentric particle ejection and the rotation of the whole fluid around the vertical axis. This base motion is of much lower frequency than the observed lateral fluctuations due to flow-induced wake instabilities. Note that the angular revolution of the vessel in the recorded period is typically less than 270° in circumference at the given rotation rate. Hence, the base-motion fraction could be removed such that the resulting path corresponds to the trajectory that an observer would see in a co-rotating frame of reference. The low-frequency part is approximated by a third order polynomial fit to the measured trajectory in three dimensional space. The resulting special curve is used to compensate for this by subtracting the functional values from the measured trajectory. This procedure was tested on synthetic trajectories. These were computed by superposition of both, small-amplitude high-frequency helix and large-amplitude helix with much higher wavelength, together yielding in sum to a cycloidal motion path. The removal of the large-scale motion by the above-described methods leads to the reconstruction of the small-amplitude helix. Deviations are only observed at the beginning and the end of the data set. These data are ultimately used for further analysis. Note that the same procedure is used for the data sets obtained in the experiments without background rotation. This is to compensate for any steady component of the lateral drift of the particle.

Quantification of path oscillation amplitude and shape

Due to the observation of many intermediate stages between zigzagging and spiraling particle paths, a mathod had to be found to quantify the differences for a larger number of experiments and to differentiate between these two stages in a statistic manner. Thus, a numeric measure, describing the lateral motion of the trajectories in magnitude and orientation on the horizontal plane (x-y plane), is proposed herein using the degree of anisotropy I:

$$\mathrm{I} = \frac{(\mathrm{I}_{\mathrm{xx}} - \mathrm{I}_{\mathrm{yy}})^2 + 4 \cdot \mathrm{I}_{\mathrm{xy}}^2}{(\mathrm{I}_{\mathrm{xx}} + \mathrm{I}_{\mathrm{yy}})^2} \qquad (3)$$

with the definitions of the second moments of area:

$$\mathrm{I_{xx}} = \sum_{\mathrm{i=1}}^{\mathrm{n}}(x_i - \bar{x})^2, \quad \mathrm{I_{yy}} = \sum_{\mathrm{i=1}}^{\mathrm{n}}(y_i - \bar{y})^2 \;, \quad \mathrm{I_{xy}} = \sum_{\mathrm{i=1}}^{\mathrm{n}}(x_i - \bar{x})\,(y_i - \bar{y}) \qquad (4)$$

The measure of anisotropy I varies between a value of 0 for a perfect circular motion in the horizontal projection and a value of 1, which is a perfect zig-zagging motion along a line in the horizontal projection, see *Jähne*[23]. Additionally, the amplitude of oscillation is introduced as a second measure to characterize the lateral motion assuming a harmonic motion. This amplitude R is determined as follows:

$$\mathrm{R} = \left[1 + \left(\sqrt{2} - 1\right) \cdot I^{0.44}\right] \cdot \sqrt{\mathrm{I_r}}\,, \quad \text{with polar moment } \mathrm{I_r} = \left(\mathrm{I_{xx}} + \mathrm{I_{yy}}\right)/\mathrm{n} \qquad (5)$$

I_r. In this context the classic formula for the polar moment has been normalized by the number n of points associated with the recorded steps in the trajectory. The preliminary factor on the right-hand side of the equation results from a fit applied to synthetic data to achieve the result of a constant lateral excursion; whereas the minor axis can vary from maximum equal to the major axis (circular path) down to zero (zig-zag path). The value of R is therefore a relevant length scale of the path excursions in the radial plane. It provides the same value if it is a helical path or zig-zagging path of the same lateral excursion. This has been tested using a synthetic dataset, assuming the horizontal projections of trajectories display certain elliptic shapes of differing ratios between the minor and the major axis β, see Figure 3.

The test calculations show the indirectly proportional relation between β and I (Figure 3b) and the approximately constant value of R in relation to β.

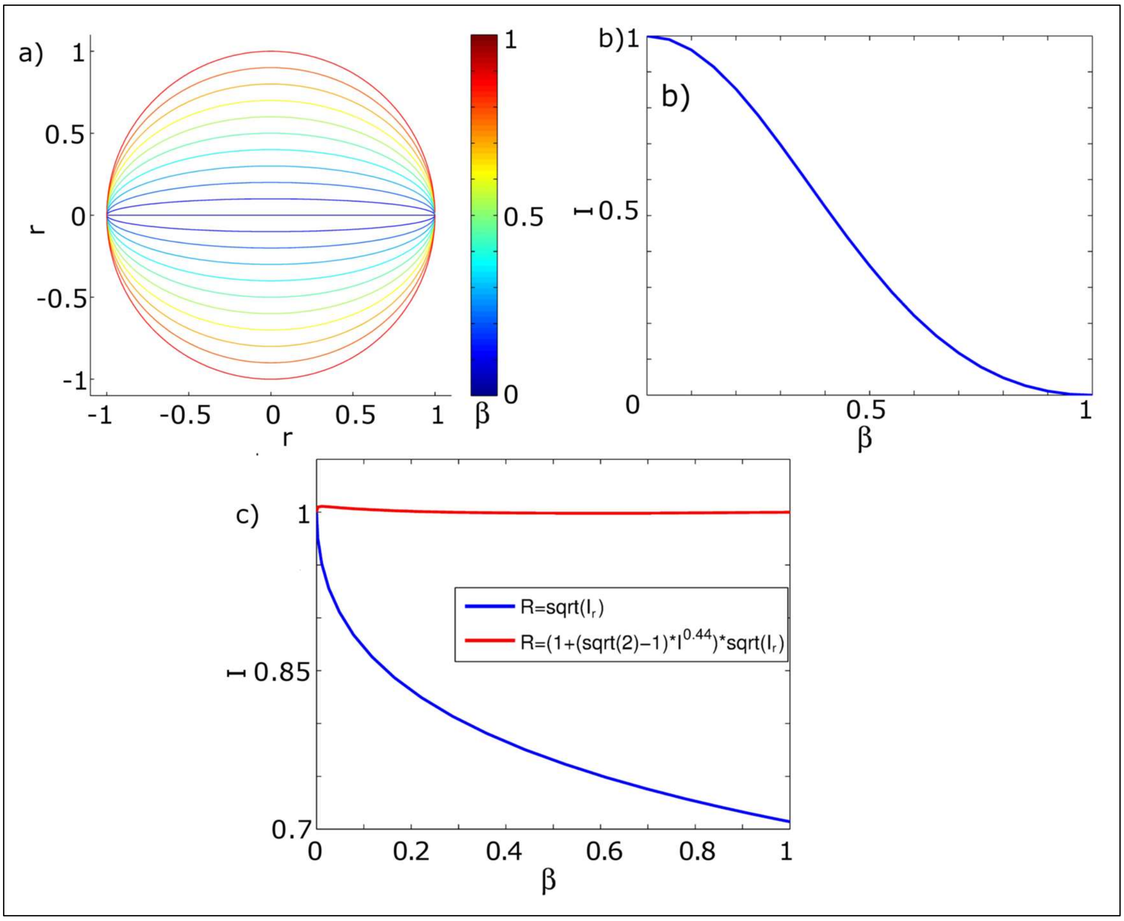

Figure 3. Test calculations of I (subimage b) and R (subimage c), assuming horizontal projections of trajectories of elliptic shapes with several ratios of the semi minor axis β while the major axis length is kept constant (subimage a).

IV.Experimental Observations

a. Slip velocities

Figure 4 illustrates the observed terminal rise velocities by means of the non-dimensional Reynolds number. Every trajectory measurement of every particle was repeated 12 times. There seems to be a slightly lower mean rise velocity with background rotation. Since this tendency lies within the standard deviation, it is not considered to be significant. If the reference case is considered without background rotation, the particles often follow a clearly zigzagging trajectory in the investigated Reynolds number range, but due to the extremely sensitive nature of the instability transitions, different transitional stages were observed even in the repetition tests. While air bubbles are known to go over to a spiraling path after, or even omitting the Zig Zagging stage, the computations of *Jenny et. al.*[19] showed mainly chaotic three-dimensional movement for solid spheres with Galilei numbers higher than 200.

The observed stages range from well-defined zig-zagging to rather ellipsoidal oscillation; where the planar, or near-planar, oscillation seems to be predominant. These variations might possibly be affected by the ejection process. Similar sensitivity was reported for bubbles by *Wu*[20], who observed that the method of bubble production had an influence on the observability of zig-zagging bubbles. He also found that the zig-zagging was only observed using a nearly momentum free ejection method (referred to as "gently push").

For the discussion of the slip velocities a set of eight trajectories, one for each of particles A-H was selected. Figure 5 shows the horizontal and 3-dimensional projections of the trajectories, along with the horizontal and vertical velocity components. The time was made non dimensional with a terminal velocity u_t and a particle diameter D.

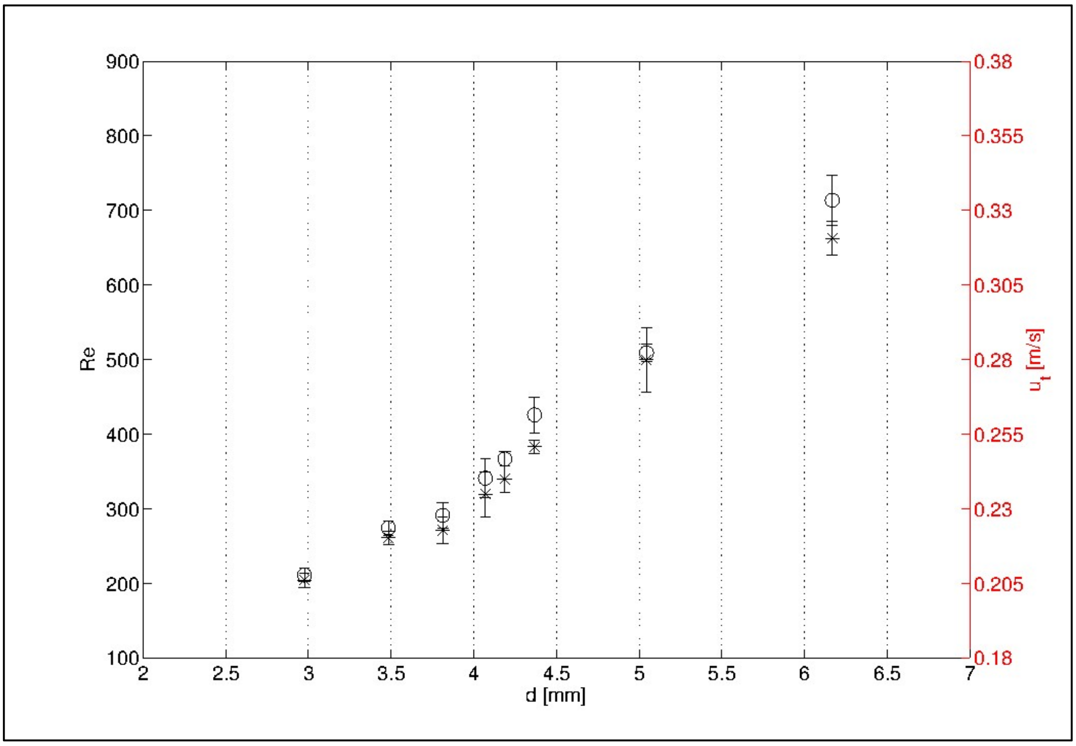

Figure 4. Reynolds number dependency on the particle diameter with (*) and without background rotation (o), including standard deviation computed for the set containing 12 repetitions. The given Reynolds numbers correspond to the terminal velocities shown on the secondary axis.

In addition to slow lateral motion (for example in the case of particle E), all trajectories exhibit clear symmetry along a vertical plane, which seems to be oriented randomly. If the horizontal slip velocity corresponding to the zig-zagging motion is considered a regular structure is obtained. The velocity amplitudes, both horizontal and vertical seem to be clearly linked to the occurring Reynolds and Galilei numbers in a directly proportional manner. The maximum horizontal velocity magnitudes are roughly one half of the terminal rise velocities. The fluctuation of the vertical velocity component is weak, and the amplitudes seem to be irregular for the lower Reynolds number experiments, but increases in amplitude proportionally to the Reynolds number. Its oscillation frequency is roughly double the horizontal oscillation frequency.

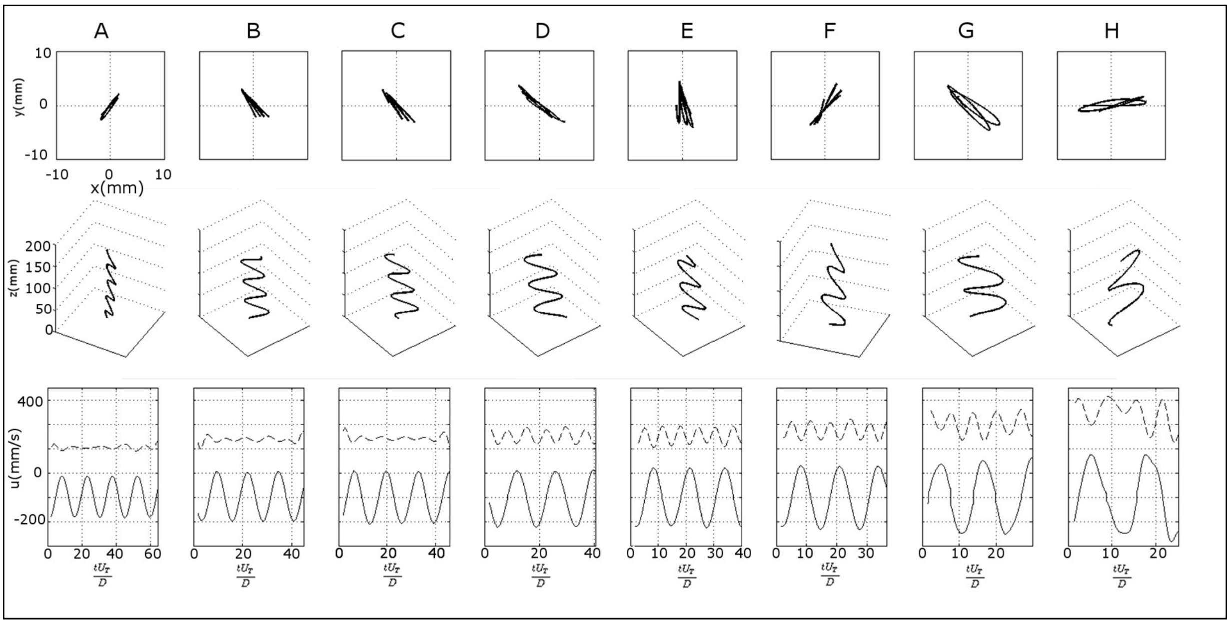

Figure 5. Exemplary horizontal trajectories (First row), 3D trajectories (second row) and slip velocities in the horizontal plane (solid lines) and the vertical direction (dashed line) in row 3 for the reference case without background rotation for particle A-H. The data correspond to terminal Reynolds numbers Re_T (Galilei numbers) of 181 (130), 290 (223), 288 (210), 362 (250), 396 (262), 430 (295), 577 (402), 850 (545).

For the case with background rotation another seven trajectories, one for each of the particles A-G, had been selected. The conducted experiments yield trajectories with differing equivalent radius (obtained by fitted circles onto the horizontal projection of the trajectory). The scale of fluctuations lies between orders measured in the experiments without background rotation (~1D) and approximately 7D, where D is the particles radius.

An explanation for these fluctuations is found in the probably unstable rotation axis, which results in varying distances from the ejection point to the center of the vortex. Thus the ejected particles experience different ambient velocity fields in relation to their relative position. To allow a qualitative discussion of the occurring horizontal slip velocities, the assumption has to be made that the center of the equivalent circle with R_{eq} coincides with the center of rotation.

Initially the influence of these differing trajectory radii are examined. Figure 5 shows the horizontal projections of the experiments with particle E at Reynolds 310.

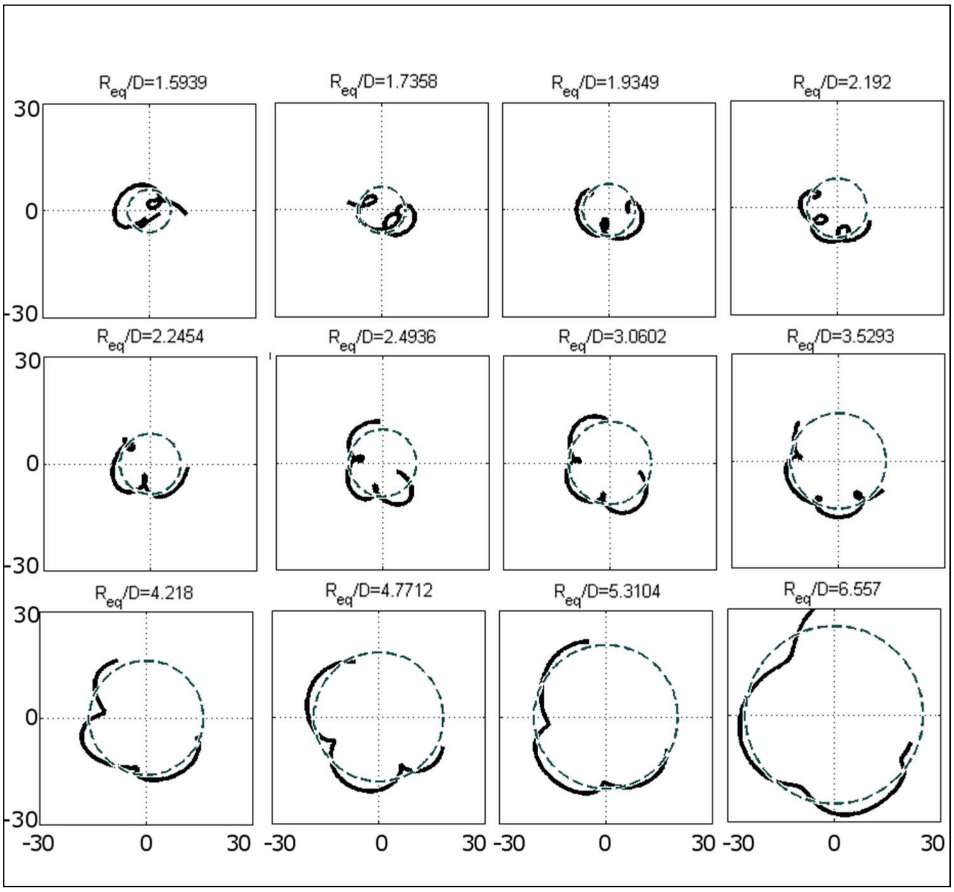

Figure 6. Horizontal projections of the trajectories of particle E (solid lines), along with the equivalent trajectory radius R_{eq}/D (dashed line).

The general shape of the observed trajectories with background rotation is cycloid-like and shows the previously mentioned superposition of two oscillating movements. The large scale oscillation coincides with the fluid rotation which entrains the particle while it is rising. The second small scale oscillation is due to occurring path instabilities, which are expressed as indentations or loops. Trajectories of larger equivalent radiusues exhibit smooth indentations, which are pointing towards the center of rotation, resulting in the shape of a shortened cycloid. With declining equivalent radius these indentations become sharper ultimately becoming a looping trajectory or extended cycloidal movement – the extreme case of this movement is a helix-shape without any large-scale oscillation. In the experiments with Particle E, these extreme stage of pure spiraling was not observed. Presuming helical movement onto a circular trajectory, the occurrence of loops depends on the velocity of the circular movement and the oscillatory frequency. With increasing circular velocity the helical movement just expresses itself as increasingly smoother indentations, assuming a constant helical frequency. Figure 6 shows an exemplary set of trajectories and slip velocities of particles A-H, corresponding to equivalent diameters $R_e/D \sim 3$.

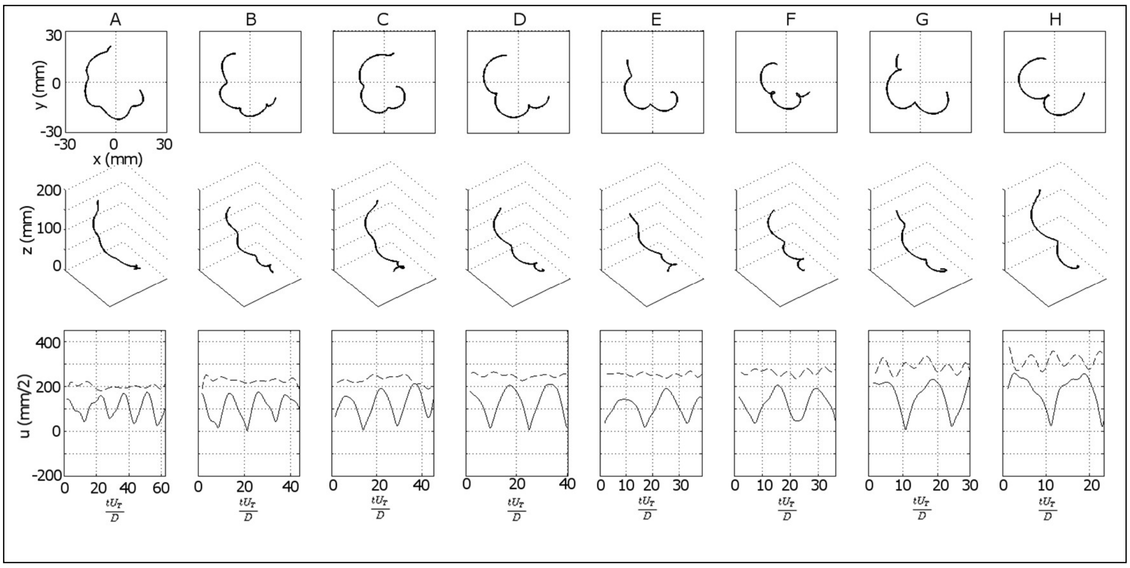

Figure 7. Exemplary horizontal trajectories (First row), 3D trajectories (second row) and slip velocities i the horizontal plane (solid lines) and the vertical direction (dashed line) in row 3 with background rotation for particle A-H. The data correspond to terminal Reynolds numbers Re_T (Galilei numbers) of 191 (130), 270 (223), 279 (210), 330 (250), 355 (262), 416 (295), 549 (402), 762 (545).

As discussed previously, the occurring path oscillations are expressed as more or less smooth indentations in the particles trajectories. The oscillation of the horizontal velocities consists of radial and circumferential fractions. Herein the circumferential part of the slip velocity is computed by $U(r)_{\varphi,slip} = U(r)_\varphi - u(r)_\varphi$, where the index φ denotes the tangential velocity component, $U(r)_\varphi$ the measured tangential particle speed and $u(r)_\varphi$ the computed background velocity. The frequencies of the horizontal slip velocities are fairly similar to the ones of the reference case; although the oscillatory movement appears to be less regular. Thus, the horizontal slip velocities minima coincide with the position of the indentations, or in case of particle F with a loop. The Amplitude range of the velocity fluctuations appears to be slightly decreased compared to the reference case. For example the oscillation range for particle A (figure 6 A) was approximately 200 mm/s; this reduces to well over 100 mm/s for the shown case with background rotation (Figure 7 A). The fluctuations of the vertical velocity component also occur with background rotation. However the onset of distinct oscillations is delayed from Re_T=362 (see Figure 5 D) to Re_T=416 (Figure 6 F).

Figure 8 shows an exemplary trajectory for particle E superposed on the velocity field of the background rotation and the radial and circumferential components of the resulting slip velocities. The time-dependent series of the velocity components is shown in Figure 8.

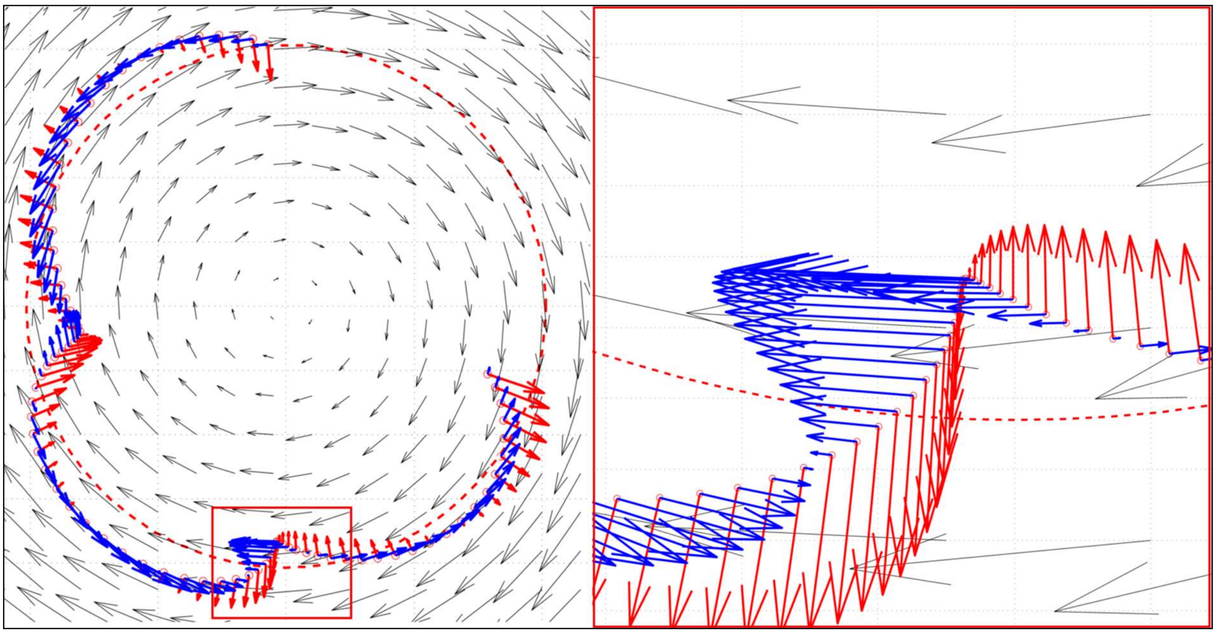

Figure 8. Trajectory of particle E with the radial (red), tangential (blue) and background velocity (black) vectors Re_T=334, R_{eq}/D=4.7 (the equivalent radius is denoted by the dashed red line).

The vector plot shows that the particle is accelerated towards and away from the center periodically. Therefore, the particle is periodically pushed into areas of higher or lower angular speeds where it is decelerated.

These velocity and path oscillations exhibit clear periodicity, which may be associated with the particles wake, whereby the presence of a planar wake structure is unlikely in this case. The calculation of the particles slip speed allows us to investigate the small scale oscillatory movement decoupled from the large scale oscillation caused by the background rotation. Figure 10 shows a trajectory of particle E (upper left side) and the corresponding phase plots of U_R and $U_{\varphi,slip}$ (upper right side). To obtain evidence of the three dimensional nature of the small-scale oscillating movement, the velocity timelines were fitted by simple harmonic functions. These were then integrated to obtain the trajectory without the influence of the large scale oscillation (lower right side). The results of these calculations are the trajectories coordinates within the horizontal plane, wherein R denotes the radial and S the circumferential direction. The phase plot of S over R clearly exhibits circulatory movement, which proves the helical shape of the small scale oscillations. In contrast to these striking difference between the particles ascent in a rotating fluid and the reference case within quiescent fluid, there appear to be no distinct differences in the general characteristics such as oscillation frequency, horizontal velocity and the oscillation amplitude, which are shown in Figure 11. In this case the frequency of the occurring velocity fluctuations was made dimensionless by applying the Strouhal number $Sr = f \cdot D/U_T$, once for the horizontal velocity oscillations (black color) and for the oscillations of the vertical velocity component (red color). The frequencies were obtained by

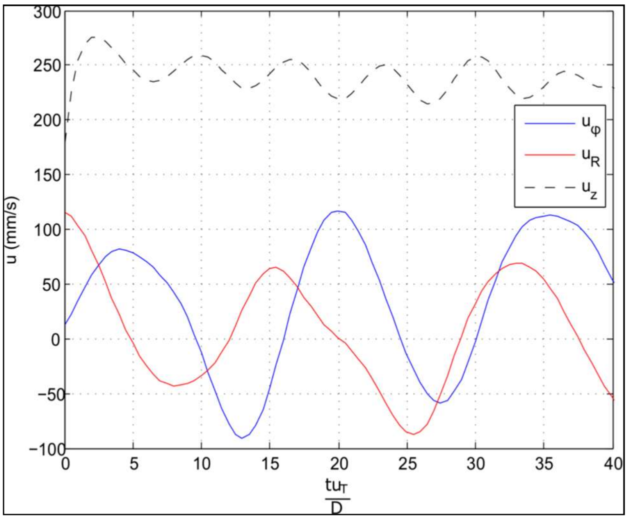

Figure 9: Vertical (dashed black line), circumferential (blue line) and radial (red line) slip velocity components corresponding to the trajectory of Particle E shown in Figure 6. Re_T=334, R_{eq}/D=4.7.

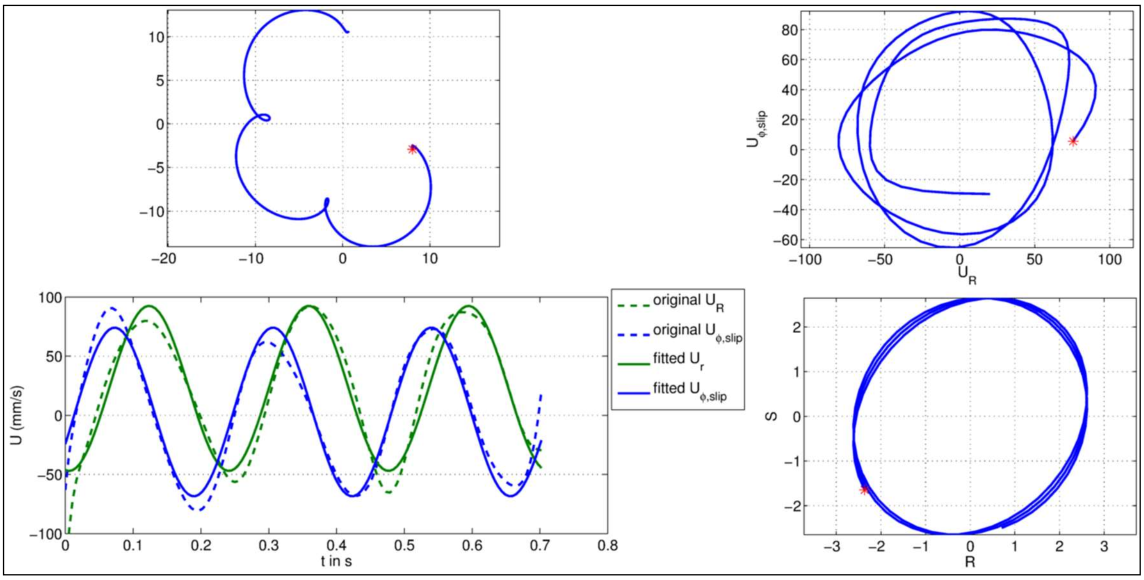

Figure 10, Trajectory of Particle E (upper left side), alongside with the phase plot of U_R in relation to $U_{\varphi,slip}$ (upper right side) and both velocity components fitted by simple harmonic functions (lower left side) alongside with the phase plot of the function integrals, denoting the integral component in Radial direction R and in circumferential direction S.

the dominant mode of the Fourier transformed velocity timelines. The non-dimensional oscillation frequencies in the horizontal plane are in good agreement with the previous findings (see *Ern et al.*[1]), which determined that the Strouhal number range lies between 0.05 and 0.1. Generally, there seems to be weak correlation with the particle diameter and not a distinct tendency for higher amplitudes within a rotating frame, especially towards higher Reynolds numbers.

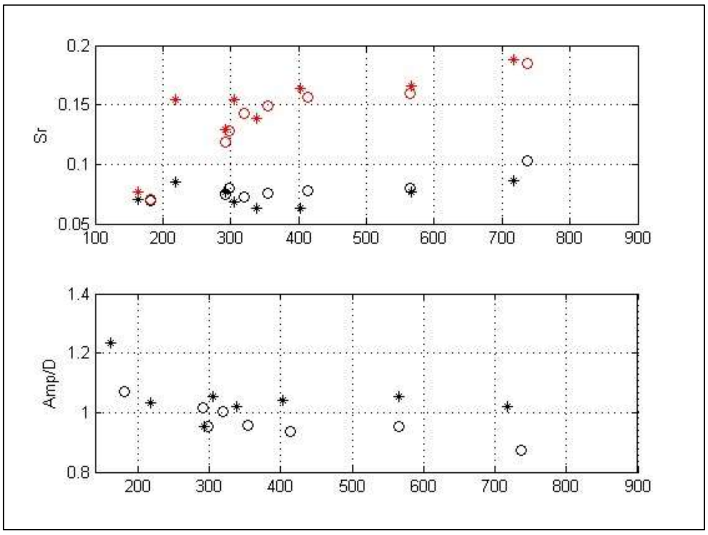

Figure 11. General Characteristics of the oscillational motion for the rotational case (*) and the reference case without background rotation (o) as function of the Reynolds number. Upper chart: oscillation frequency (made dimensionless by $Sr=fD/U_T$). Lower chart: Oscillation amplitudes normalized with the Particles diameter D. The dimensionless frequency the vertical speeds oscillation is marked up by red color

b. Statistical evaluation

The thus-far presented observations are also reflected in the measures of the anisotropy I and the oscillation radius R. These were computed for all the experiments and plotted against each other in Figure 12; in addition, a probability density function (joint PDF) is superposed to indicate the separation of the two experimental cases (with background rotation and the reference case). The PDF was calculated over all measurements contained in the variables of I and R, using a box counting method on a regular grid. In this procedure, small search-windows of ΔI, ΔR are moved stepwise along the grid axes and all measurements lying within the search-window are counted. The resulting distribution is smoothed with a 3x3 kernel, and contour lines are plotted. In the case of background rotation, the anisotropy of path oscillations varies between 0 (perfect circular) and 0.2 (ellipsoidal), whereas much larger variations are observed for the experiments in quiescent fluid where the range is from I=0.3 to nearly I=1 (pure linear oscillations). As suggested by the exemplary computation, shown in Figure 10, a clear separation of the measurements with a rotating frame and the reference case without background rotation is shown, supporting the hypothesis of an asymmetrical wake structure.

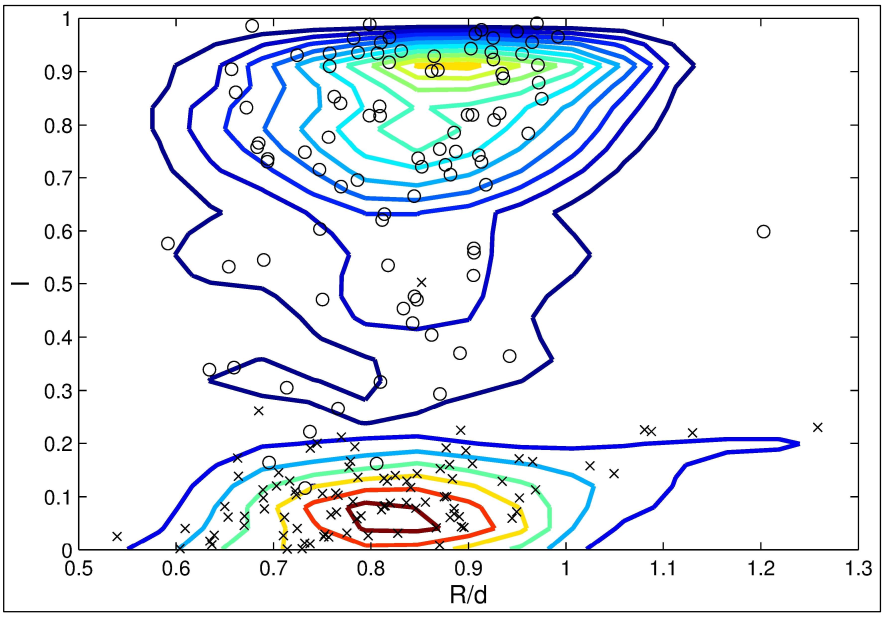

*Figure 12. Joint PDF of anisotropy I and oscillation amplitude R normalized with the particles diameter d for the investigated particle sets, containing all measurements without background rotation (*o*) and with background rotation (*x*). Superposed by contour lines indicating the probability density of the measured parameter within the investigated area (Red indicates areas of higher Probability)*

c. Wake visualization

As stated frequently throughout the literature, the observed path instabilities are probably due to the wake structure of the rising body. (see *Ern et al.*[1]) . To investigate possible crosslinks between the induced wake structures and the finding of the trajectory measurements, a wake visualization study containing stereoscopic images of the dye coated particles A-H was recorded. It must first be mentioned that the particle mass is affected by the dye coating, resulting in a possible influence on the terminal velocity and consequently on the resulting mean Reynolds number. Assuming a dye density of 1.2 g/cm³ and a layer thickness of ~80 µm, the mass of the smallest particle changes below 5%, which is not considered to be relevant for the observed path instabilities. Moreover, the measurement of the particles trajectories are not possible in the wake visualization study. Figure 13 shows the set of wake recordings for the reference case. The same set of 8 particles as in the trajectory measurements was used. The specified Reynolds numbers correspond to the mean Reynolds numbers calculated within the trajectory measurement. The pictures contain 2 stereoscopic images taken from the perpendicular viewing directions of both cameras (side and front view). The subimages A-H have been ordered corresponding to the particle numbering codes in Table 1. Figure 13 A shows the particle wake at Re= 170. According to *Horowitz et. al.*[3], the predominant regime could be characterized as oblique. Consequently, the path could not be considered to be perfectly rectilinear. Moreover, there are initial states of vortex shedding, which collaborates with *Brücker*[14,] who observed eminent wake instabilities only at Reynolds numbers over 180. With increasing Reynolds numbers, vortex shedding events appear while the two threaded wake structure observed in numerous investigations, e.g. *Veldhuis et. al.*[6], *Horowitz et. al.*[3], is omnipresent. With further increasing Reynolds number, a tendency for the progressive development of horseshoe-type vortex loops is observed. Especially subimages D-F representing Re=330, 334 and 416 illustrate that the zig-zagging plane is rotated 90° to the plane of vortex-shedding. This implies the coupling of this kind of wake phenomena to the characteristic zig-zag path oriented in a horizontal plane as concluded by *Brücker*[14]. The fact that that no definitive vortex shedding could be observed in the case of subimage B and C (Re 242 and 278) may be result of the mismatches of the camera orientations with the particles oscillation plane.

For the wake description we adhere to the classification made in *Horowitz et. al.*[3] with 1R-mode for single-sided shedding and 2R-mode for double-sided shedding of vortex loops. In addition, they observed a 4R-mode referring to the presence of one dominant and one recessive loop on each side. The observations made in the present study suggest a bifurcation from the double-threaded wake mode classified as “oblique” mode (subimage A) to 1R-mode (B, C), which then evolves into the 2R-mode (D, E) and ends in the 4R mode, clearly present above Re=380 (F, G).

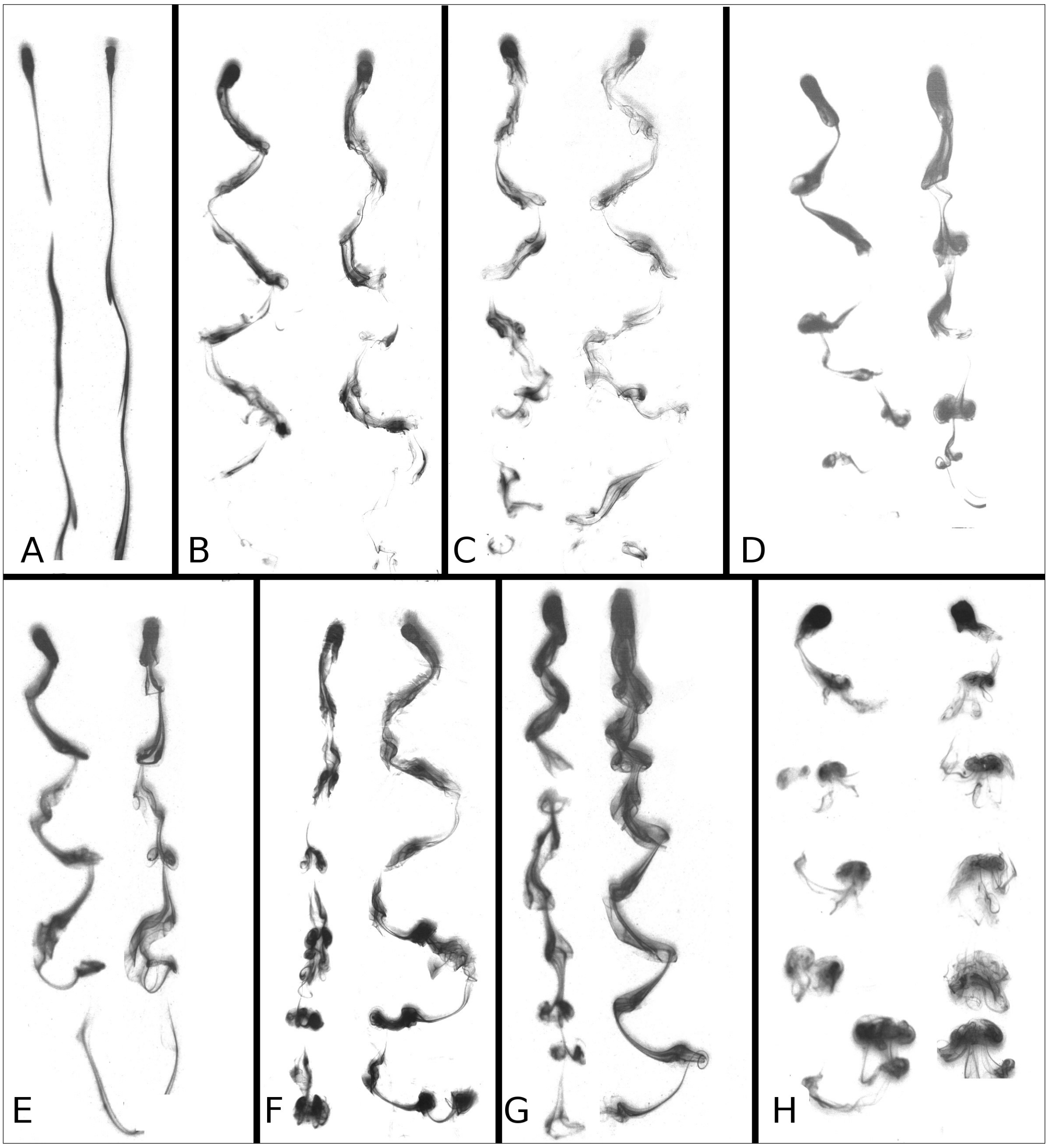

Figure 13. Wake visualizations of the particle set, sorted by ascending Reynolds number (see Table 1) in water glycerol mixture at rest. The subimages A-H represent different particle diameters (in mm); the average Reynolds numbers were obtained from the trajectory measurements and Galilei numbers.

In subimage H the stronger shear layer results in a high mixing rate between the wake regions with high dye concentration and the surrounding fluid. This renders the vortex regions more difficult to visualize; consequently, only the dominant loop-type vortex structures are seen.

Figure 14 shows the wake structures under influence of background rotation. Although there is no distinct difference between Figure 13 A and Figure 14 A, it was apparent that vortex shedding events do not become more frequent with increasing Reynolds number as in Figure 13. This tendency towards vortex shedding suppression is a definiter observation considering the wakes of identical particles in Figures 13 and 14. Instead, there is still a two threaded type of wake structure, which has also been observed in numerous experimental studies with spheres (e.g. *Brücker*[14]) or bubbles up to the Re-numbers of 300, e.g. *Sakamoto et. al.*[21], *DeVries et. al.*[5] or *Veldhuis et. al.*[6]. Aside from small disturbances, the two counter rotating vortices appear to remain stable in the rotating background (see Figure 13 subimages B-F) up to Re≈500.

The areas marked with ellipses in Fig. 14 indicate that crossings oft the wake patterns frequently occur. Taking the fixed camera position and the fact that the observation time covered less than one complete rotation of the cylinder into account, these crossings have to be subject to a rotation of the primarily two-threaded wake structure behind the rising particle. Consideration of the trajectory study indicates that the more regular wake structure corresponds to the predominant spiraling path of the trajectories.

The regular vortex structure appears to still be existent, which is also implied by the prevailing vertical velocity oscillations (see Figure 7).

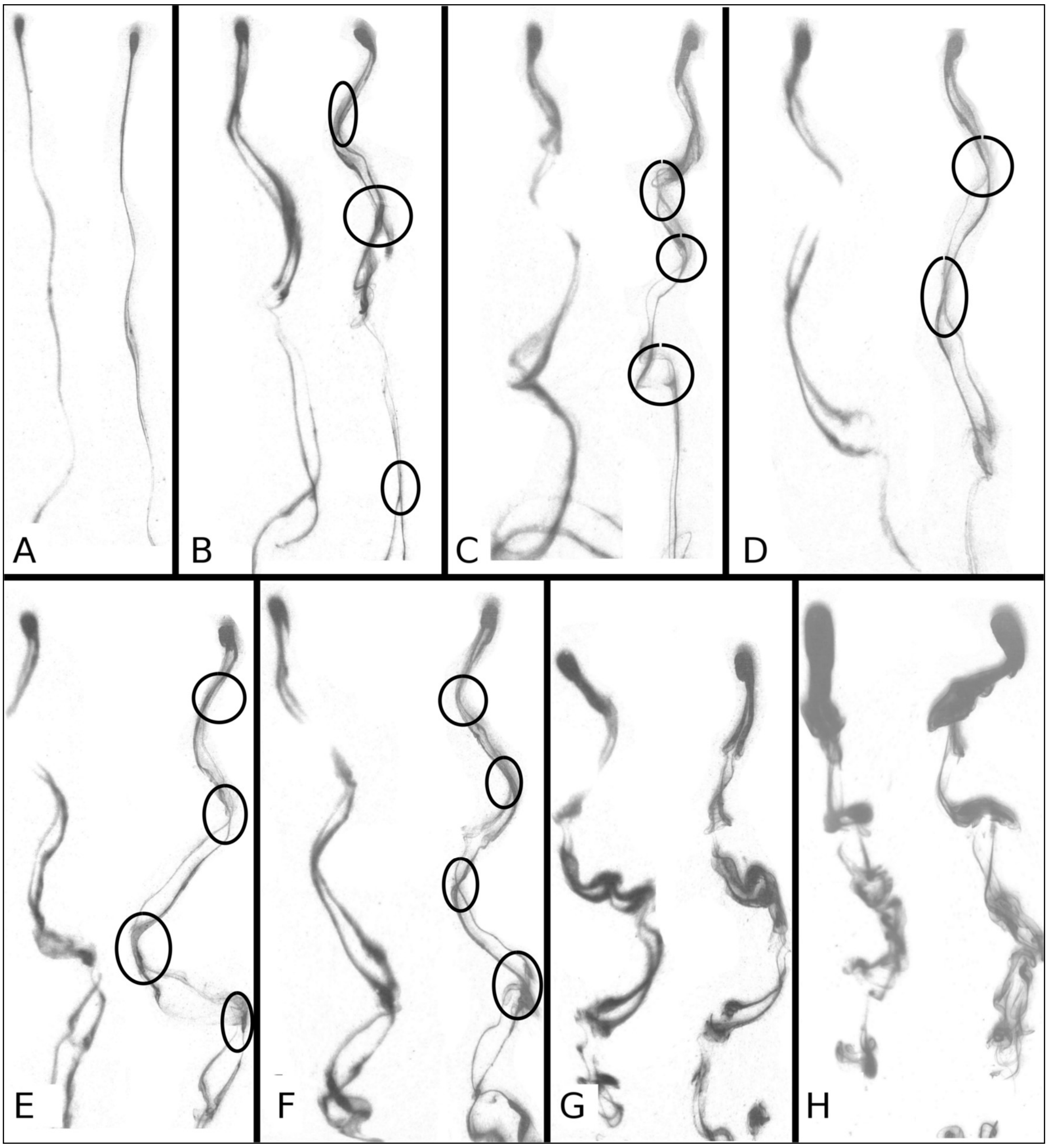

Figure 14. Wake visualizations of the particle set, sorted by ascending Reynolds number (see Table 1) in a water glycerol mixture in a rotational frame (ω=0.815 1/s). The subimages A-H represent different particle diameters (in mm); the average Reynolds numbers were obtained from the trajectory measurements.

V.Conclusion

In the present study both trajectory measurements and wake visualizations were pperformed for light particles rising in a water-glycerol mixture both at quiescent flow conditions and with background rotation. Polystyrene particles with density ratios lower than 0.07 were used. The equivalent particle diameters ranged from 2-6 mm, yielding average Reynolds numbers between 177 and 800. The measurements were performed using a stereo-shadowgraphy setup consisting of two cameras oriented perpendicular to each other. The trajectory measurements reveal that the transition from rectilinear/oblique to zig-zagging to spiral movement is a highly sensitive process. For example, the measurements showed many different transitional stages during the 12 repetitive measurements for every particle,. Although the zig-zagging mode appears to be dominant under quiescent conditions. These zig-zagging paths correspond to a regular oscillation of the horizontal slip velocities and an oscillation of the vertical velocity component at roughly twice the horizontal frequency. These vertical oscillations are amplified with increasing Reynolds number. The amplitudes of the path oscillations appear to decline with increasing Reynolds number from roughly 1.1 particle diameters at Re_T=190 to approximately 0.9 for Re_T=730. This might correspond with the occurrence of further wake modes, for example at the transition from 2R to 4R mode.

Regarding the rise in a slowly rotating frame, the observer, who is co-rotating with the reference frame, sees predominantly spiraling ascents. This observation was tested by exemplary calculations using the horizontal slip velocity components to show characteristic phase shifts between the radial and circumferential slip velocities. Furthermore, a statistical approach had been chosen to support this general observation. Measures of lateral oscillation anisotropy and amplitude were computed for all data. These calculations demonstrate a clear separation of the two basic experimental conditions. The different tendencies observed in the trajectory measurements are supported by the wake visualization studies. Visualizations in the reference case show a clear transition from a smooth double-threaded wake structure that develops vortex shedding with increasing Reynolds number from 1R to 2R and 4R-mode. The observed vortex shedding structure of the experiments in quiescent fluid are in good agreement with, e.g., *Horowitz et. al.*[3], and it is obvious that the horizontal plane in which vortices are shed is rotated approximately 90 degrees (horizontal) to the zig-zagging plane. In contrast to these observations, the experiments with a rotating frame indicate a dominant two threaded wake structure that prevails over a large Reynolds number range up to 500, at which vortices began to be shed; although the vertical velocity fluctuations are still existent and have the same order of magnitude that was observed under quiescent conditions. The measured trajectories for the case of background rotation were arranged according to their equivalent trajectory radius, which fluctuated throughout the experiments. These fluctuations of the particles' orbits are most likely due to an unstable rotation axis. These differing trajectory radii seemed to have no distinct influence on the path instability parameters, although the trajectories' shapes varied if different equivalent trajectory radii were considered. For small equivalent radii the path oscillations are shown to be clear distinctive loops that become increasingly smooth indentations with increasing equivalent radius. Given the fact that, in contrast to the reference case, no definite vortex shedding, was observed even though the path instabilities are still persistent, the wake structure must have lost its planar symmetry. A common explanation would be a periodic rotation of the observed two-threaded wake structure with the same frequency as that measured for path instabilities under quiescent conditions. This assumption is supported by frequently observed crossings of the occurring double-threaded wake structures. The presence of background rotation delays the onset of vortex shedding to higher Reynolds numbers and stabilizes the wake. Note that the present results apply only to the given parameter set of solid particles at density ratios below 0.07 and swirl ratios of Ro=57…95. Further experiments are necessary in a larger variation of the parameter space of Ro to quantify the transition point in more detail. In addition, quantitative flow measurements of the wake using PIV might help to understand the modification of the wake. The first indications of the relevance of swirl on wake stabilization of flow around a solid sphere were already shown in *Rudert et. al.*[22].

VI.Acknowledgments

The funding of the project by the German Research Foundation within the project BR 1494/24 is gratefully acknowledged.

Professor Christoph Bruecker is currently BAE Systems Sir Richard Olver Chair in Aeronautical Engineering, City University London, whose support is gratefully acknowledged.

VII.References

[1] Patricia Ern, Frédéric Risso, David Fabre and Jacques Magnaudet (2012): *Wake-Induced oscillatory Paths of Bodies Freely Rising or Falling in Fluids.* Annu. Rev. Fluid. Mech. **44**, p. 97-121

[2] T.R. Auton, J.C.R. Hunt, M. Prud'Homme, (1988): *The force exerted on a body in inviscid unsteady non-uniform rotational flow.* J. Fluid Mech. **197**, p. 241-257

[3] M. Horowitz, C. Williamson, (2010): *The effect of Reynolds number on the dynamics and wakes of freely rising and falling spheres.* J. Fluid Mech. **651**, p. 251-294

[4] J. Magnaudet, G. Mougin (2007): *Wake instability of a fixed spheroidal bubble*. J. Fluid Mech. **572**, p. 311-337

[5] A. DeVries, A. Biesheuvel, L. van Wijngaarden (2002): *Notes on the path and wake of a gas bubble rising in pure water.* In Int. J. of Multiphase Flow, **28**, p. 1823-1835.T.

[6] C. Veldhuis, A. Biesheuvel, L. Van Wijngaarden, D. Lohse, (2005): *Motion and wake structure of spherical particles.* Nonlinearity **18** (1), p. C1-C8.

[7] C. Veldhuis, A. Biesheuvel, (2007): *An experimental study of the regimes of motion of spheres falling or ascending freely in a Newtonian fluid.* International Journal of Multiphase Flow **33** (10), p. 1074–1087.

[8] T. Sarpkaya, (2001): *On the force decompositions of Lighthill and Morison.* J. of Fluids and Structures **15**, 227-233

[9] G. Sridhar, J. Katz (1995) *Drag and lift forces on microscopic bubbles entrained by a vortex.* Phys. Fluids **7**, p. 389-399.

[10] P. Bagchi, S. Balachandar, (2002) *Shear versus vortex-induced lift force on a rigid sphere at moderate Re.* J. Fluid Mech. **473**, p. 379-388.

[11] J. Bluemink, D. Lohse, A. Prosperetti, L. Van Wijngaarden, (2010): *Drag and lift forces on particles in a rotating flow.* J. Fluid Mech. **643**, p. 1.-31

[12] K. Ellingsen, F. Risso, (2001): *On the rise of an ellipsoidal bubble in water. Oscillatory paths and liquid-induced velocity.* J. Fluid Mech. **440**, p. 235-268

[13] W. Shew, S. Poncet, J. Pinton (2006) *Force measurements on rising bubbles.* J. Fluid Mech. **569**, p. 315-534.

[14] C. Brücker (1999) *Structure and dynamics of the wake of bubbles and its relevance for bubble interaction.* Phys. Fluids **11**(7), p. 1781-1796.

[15] C. Brücker (2001) *Spatio-temporal reconstruction of vortex dynamics in axisymmetric wakes.* Journal of Fluids and Structures **15** (3-4), 2001, p. 543-554.

[16] G. Settles, (2010): *Important developments in schlieren and shadowgraph visualisation during the last decade.* 14th International Symposium on Flow Visualization. Daegu, Korea, June 21-24.2010

[17] S. Soloff, R. Adrian; Z. Liu, (1997): *Distortion compensation for generalized stereoscopic particle image velocimetry.* Meas. Sci. Technol. **8** (12), p. 1441-1454.

[18] M. Kühn, (2011): *Untersuchung großskaliger Strömungsstrukturen in erzwungener und gemischter Konvektion mit der tomografischen Particle Image Velocimetry.* Doctoral Thesis. Ilmenau

[19] M. Jenny, J. Dusek, G. Bouchet (2004): *Instabilities and transition of a sphere falling or ascending in a Newtonian Fluid.* J. Fluid Mech. **508**, p. 201-239

[20] M. Wu, M. Gharib, (2002): *Experimental studies on the shape and path of small air bubbles rising in clean water*. In Phys. Fluids **14** (7), p. L49.

[21] H. Sakamoto, H. Haniu, (1990): *A Study on Vortex Shedding From Spheres in a Uniform Flow.* Trans ASME J. Fluids Eng. **112** (4), p. 386-392

[22] A. Rudert, H. Chaves, C. Brücker: (2006) *Effect of background rotation on the structure of sphere wake flow.* Proc. Europ. Fluid Mechanics Conference 2006, Stockholm.

[23] B. Jähne: *Digitale Bildverarbeitung und Bildgewinnung* (Monografie), Springer Verlag, Berlin, 2012